



# Aeroelastic Analysis of a Wind Turbine with a Bamboo Honeycomb Structural Web

T. Su, K. Chen<sup>†</sup>, Q. Wang, Z. Zhao and H. Hu

*College of Mechanical Engineering, Xinjiang University, Urumqi 830046, China*

<sup>†</sup>Corresponding Author Email: [chenkun@xju.edu.cn](mailto:chenkun@xju.edu.cn)

## ABSTRACT

As the size and flexibility of wind turbine blades increase, the aeroelastic challenges faced by wind turbines become more pronounced. To prevent blade damage due to vibration and improve the aeroelastic stability of wind turbine blades, this paper proposes a bionic blade with a bionic web inspired by bamboo and honeycomb structures. The fluid-solid interaction analysis of the blades is conducted using computational fluid dynamics and the finite element method, based on the Shear Stress Transport (SST)  $k-\omega$  turbulence model. The displacements, stresses, strains, modal, and harmonic response analyses of both the original and bionic blades are evaluated under rated operating conditions. The results indicate that, compared to the original blade, the maximum displacement of the bionic blade is reduced by 10.1%, the maximum stress value on the blade surface is 2.1% lower, and the maximum strain value is 2.5% lower. The bamboo honeycomb web buffers wind loads in stages during the vibration and deformation of the bionic blade, leading to reduced vibration displacement and improved deformation resistance.

## Article History

*Received November 13, 2024*

*Revised March 10, 2025*

*Accepted March 28, 2025*

*Available online June 3, 2025*

## Keywords:

*Numerical calculation*

*Bionic structure*

*Fluid-solid interaction*

*Modal analysis*

*Vibration*

## 1. INTRODUCTION

With the world's increasing focus on clean energy, wind energy technology has evolved rapidly over the past few decades. Larger, lighter, and more flexible blades enable greater efficiency at minimal cost (Shehata et al., 2024). The role of blades in wind turbines should not be overlooked. During the development of horizontal-axis wind turbines, blades became more flexible, stiffness decreased, the shape became elongated, and blade deformation increased. These changes can cause wind turbine destabilization, breakage, and other problems. The problem of aeroelasticity caused by the loads imposed by air impingement on the blades is likewise worthy of attention (Zhang et al., 2024). The vibration and deformation of blades under strong wind loads not only affect power generation efficiency but may also lead to structural damage or even failure. Therefore, improving the aeroelastic stability of blades and reducing vibration and deformation have become key challenges in wind turbine design. To ensure safe blade operation, aeroelastic analysis is an indispensable part of blade design.

To study the aeroelastic behavior of blades, scholars have developed various numerical analysis methods over the years. One widely used method is fluid-solid interaction. This method has been recognized in studies

involving fluid interaction with solids and has been applied to blade analysis (Keprate et al., 2023). Wang et al. (2016) simulated a WindPACT 1.5 MW wind turbine using unidirectional fluid-solid interaction. The maximum stress and tip deflection were obtained for each case based on five operating conditions, with each result falling within material and structural limits. Wang et al. (2023) analyzed the aeroelasticity of the NREL 5 MW wind turbine using two-way fluid-solid interaction, demonstrating that a wind turbine with a web is more stable. Zheng et al. (2022) examined the aeroelasticity problem at various levels of turbulence intensity using two-way flow-solid interaction, finding that blade aeroelasticity issues become more pronounced with increasing turbulence intensity. Zhang et al. (2023) investigated the structural aspects of an IEA 15 MW wind turbine under the combined effects of wind loads and ocean forces using unidirectional fluid-structure interaction, showing that waves significantly impact turbine performance. Huang et al. (2024) proposed a new fluid-solid interaction model to simulate real-world turbine conditions by applying various loads to the model, revealing that wind turbine deformation influences wake flow. Yassen et al. (2023) compared unidirectional and bidirectional fluid-solid interaction in GE 1.5-XLE wind turbine blades, demonstrating the accuracy and efficiency of fluid-solid interaction analysis by evaluating relative

errors. [Li et al. \(2023\)](#) used a fluid–solid interaction method to study wind turbine behavior, showing that the presence of a tower increases turbine output power.

Advancements in aerodynamic design and materials science have enabled the scaling of horizontal-axis wind turbine (HAWT) blades to megawatt-class dimensions. However, this increase in scale amplifies bending moments and fatigue loads due to larger rotor-swept areas. Ensuring safe wind turbine operation has become a key concern for scholars. Some researchers aim to enhance blade safety by modifying blade structures or adding devices. [Shalini Verma et al. \(2022\)](#) increased wind turbine power by installing winglets. Using unidirectional fluid–solid interaction, they analyzed aeroelasticity under three different tip-speed ratios and two materials, finding that blade deformations and stresses remained within the allowable range. [Huang et al. \(2022\)](#) designed a bionic wing inspired by dolphin bones, studying blade noise and rotation. The results showed minimal noise increase while torque improved, inhibiting flow separation. [Huque et al. et al. \(2024\)](#) examined three different wind turbine tip shapes (NREL Phase VI), analyzing blade stress and deformation. Their findings indicate that modifying blade tips enhances power generation while maintaining structural integrity.

In addition to structural modifications, blade stability can also be improved by altering materials to enhance strength.

[Deng et al. \(2024\)](#) proposed a generalized fluid–solid interaction framework for analyzing composite blades, improving computational efficiency under the same conditions. [Choi et al. \(2022\)](#) examined blade skinning, comparing intrinsic frequency and vibration patterns. [Barr & Jaworski \(2019\)](#) developed variable-angle filament bundle composite wind turbines, achieving a 14% increase in power output. [Torregrosa et al. \(2022\)](#) designed two composite layup structures, showing that one configuration increased critical wind speed by 10%.

The field of wind turbine design has advanced significantly through biomimetic principles, drawing inspiration from nature to enhance performance, efficiency, and durability. Researchers have explored various bionic structures and systems to address challenges such as vibration, deformation, and fatigue in wind turbine blades. For instance, [Herrera et al. \(2019\)](#) developed a biomimetic HAWT inspired by the aerodynamic morphology of *Triplaris Americana* seeds. This turbine not only improved wind energy conversion efficiency but, after optimization, also reduced blade deformation during normal operation. [Zhao et al. \(2024\)](#) designed a bionic wind turbine blade inspired by owl feathers, showing improved vibration performance that enables better adaptation to severe wind field environments. [Liu et al. \(2022\)](#) evaluated two honeycomb web structures for blade design, using numerical simulations to confirm their effectiveness in enhancing mechanical properties. [Zheng et al. \(2023\)](#) proposed a bionic plate design based on beetle forewings, significantly reducing weight while maintaining high strength, with improved fatigue resistance. In contrast to the bionic structures mentioned above, the bionic principle

of the bamboo honeycomb web in this study is based on bamboo and honeycomb structures. Bamboo features high toughness, low weight, and high compressive strength, while honeycomb structures offer excellent impact resistance, heat dissipation, and shock absorption properties. In this study, the internode structure of bamboo and the honeycomb structure were applied to the blade web design, enhancing aeroelastic stability. The bionic web structure effectively buffers wind loads, reduces blade vibrations, and improves resistance to deformation.

Bamboo's unique properties, such as a high strength-to-weight ratio, excellent toughness, and a natural ability to withstand dynamic loads, make it ideal for wind turbine blade bionic applications. The honeycomb structure, known for its high strength and stability, further enhances the mechanical properties of the blade. By combining these two natural structures, a novel bionic web design is proposed, where the two structures are effectively applied to wind turbine webs. This approach innovatively integrates the spatial distribution pattern of bamboo joints with the honeycomb structure to enhance the mechanical properties of the blade web.

Research by the aforementioned scholars demonstrates that most studies analyze wind turbine blade issues using the fluid–solid interaction method. Some scholars modify the blade structure by adding devices to optimize aeroelastic performance, while others analyze stress and deformation during operation to prevent blade damage due to excessive deformation. Composite materials are also employed to improve blade stability. In this paper, a bionic web plate is proposed by incorporating the bionic structures of bamboo and honeycomb into the web plate. The aeroelastic performance of the blade is then analyzed by applying this bionic web plate to the wind turbine blade. This study not only addresses the aeroelastic challenges associated with increasing blade size and flexibility but also highlights the significant potential of bionics in engineering design. The biomimetic honeycomb architecture of bamboo provides inherent resilience to mechanical loads, enabling wind turbine blades to endure extreme operational stresses such as high winds and turbulence. The biomimetic blade design minimizes loads such as deformation and stress concentrations, thereby enhancing the operational durability and failure resistance of wind turbines. In addition, the integration of bamboo and honeycomb structures into the bionic design offers an innovative approach to wind turbine blade engineering. This design reduces wind turbine maintenance costs and, from a broader perspective, contributes to the advancement of renewable energy technologies by lowering overall turbine costs.

This paper focuses on the following topics: first, an introduction to the original blade and the bionic blade, followed by the design of a bionic web based on bamboo and honeycomb. A numerical simulation of wind turbine operation was conducted, comparing the deformation, stress–strain response, modal analysis, and harmonic response of the original and bionic blades. Comparative analyses reveal that the nature-inspired blade significantly outperforms traditional blades in deformation resistance,

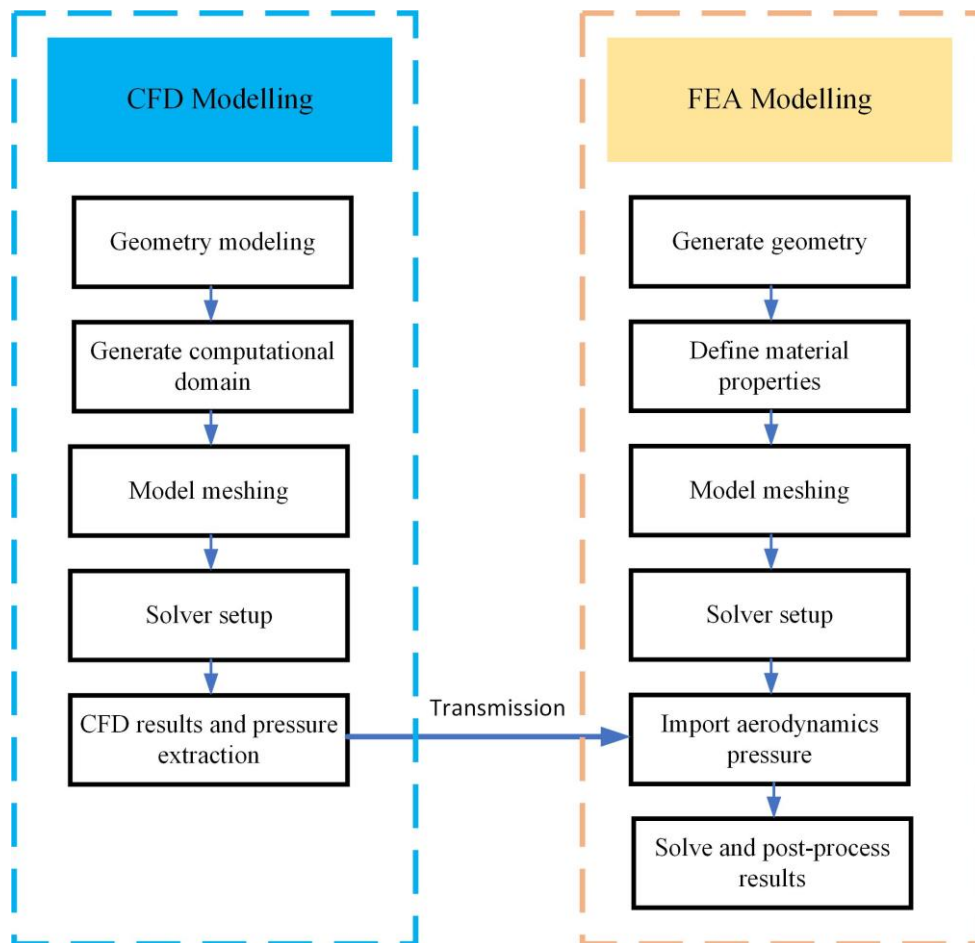


**Fig. 1 One-way FSI modeling schematic**

stress distribution, and vibration response, verifying the effectiveness and practicality of the bionic web design.

## 2. METHODS

### 2.1 One-Way Fluid-Solid Interaction

One-way fluid-structure interaction can significantly reduce computational time and resource consumption while maintaining computational accuracy, particularly in large wind turbine blade simulations. The one-way fluid-structure interaction (FSI) model has been validated for its precision in wind turbine blade simulations by Wang et al. (2016), who also noted its widespread adoption in aeroelastic studies due to its computational efficiency. The coupling method used in this paper is one-way fluid–solid interaction. The primary objective of unidirectional fluid–solid interaction is to transfer the calculated fluid load to the solid structure as a linear static force to determine the structural deformation of the solid. In the one-way fluid–solid interaction calculation, the fluid load and temperature are first determined using the computational fluid dynamics (CFD) method. When the flow field solution meets the convergence criterion, the computed aerodynamic load on the blade is transformed into boundary conditions. This aerodynamic load is then transferred to the solid structure via the coupling interface, after which the finite element computational method is used to analyze the blade model under aerodynamic,

gravitational, and centrifugal loads. The structural response (e.g., deformation and stress–strain distribution) of the blade model under these loads is then calculated using finite element analysis. Figure 1 presents the flow diagram of the fluid–solid interaction process.

### 2.2. Wind Turbine Model

#### 2.2.1 Original Blade

The NREL 5 MW wind turbine, widely used as a standard reference model, is recognized by the wind energy research community as an accurate prototype for comparing results across different studies. Consequently, conclusions drawn from studies using this model can be generalized to other wind turbine designs and sizes. The 5 MW wind turbine is comprehensively documented, with detailed specifications, performance metrics, and operating characteristics publicly available. This complete dataset allows for precise modeling and simulation. Accordingly, the 5 MW wind turbine is selected as the blade prototype for this study. The original model used in this paper is the NREL 5 MW wind turbine (Jonkman et al., 2009). The primary airfoils used in this wind turbine blade include the Dutch DU series airfoils and NACA 64 airfoils. The blade root features a large airfoil thickness to support greater loads, while the tip region utilizes thinner airfoils. The blade is a hollow structure with a web, where the web begins at 0.3C from the leading edge of the first DU 40 airfoil. The rated wind speed of the wind turbine is

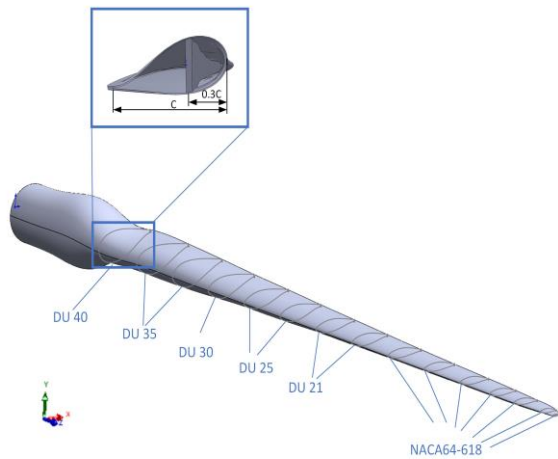


**Fig. 2** 5 MW turbine blade

**Table 1** Parameter similarity relationship

Parameter	Relativity
Impeller speed $\Omega$ /rpm	$\frac{\Omega_1}{\Omega_2} = R^{-1}$
Torque $M$ /N·m	$\frac{M_1}{M_2} = R^3$
Power $P$ /W	$\frac{P_1}{P_2} = R^2$

11.4 m/s, the rated rotational speed is 12.1 r/min, and the blade length is 61.5 m. The web and beam cap carry the torsional shear and bending moment loads of the blade. Figure 2 illustrates the 5 MW wind turbine model.

Due to the substantial size of the original 5 MW wind turbine model, computational resource optimization is necessary. To achieve this, similarity theory is applied to scale the design. The similarization process adheres to the following guidelines: first, the same blade tip-speed ratio must be maintained in both simulation conditions; second, the blade airfoil profile and the number of airfoils must remain unchanged; finally, all dimensions, including radius, chord length, and airfoil thickness, must be scaled accordingly (Giahi & Jafarian Dehkordi, 2016). In this study, the blade length of the 5 MW wind turbine is reduced by a factor of 50, with a similarity coefficient of  $R = 50$ . The similarized wind turbine has a rated speed of 605 r/min, a torque of 32 N·m, and a rated power of 2000 W. Table 1 presents the similarized parameters.

### 2.2.2 Bionic Blade

In this study, bamboo and honeycomb are selected as the original biomimetic prototypes for the web structure of wind turbines. Bamboo has excellent physical properties, is lightweight, has high toughness, and possesses high compressive and tensile strength. The honeycomb structure exhibits excellent mechanical properties, providing high strength and structural stability. It performs exceptionally well in impact resistance, heat dissipation, and shock absorption.



**Fig. 3** Bamboo joint distribution and bionic web

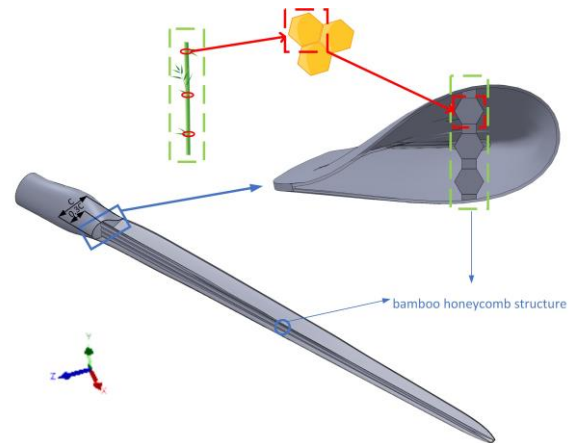


**Fig. 4** Bionic blade

In this paper, bamboo and honeycomb structures are applied to the bionic blade web. The bamboo joints enhance compressive and flexural strength while inhibiting cracking under stress conditions (Han et al., 2024). Bamboo is characterized by varying node distributions, and the web can be analogized to bamboo, allowing for the generation of nodes within the web. According to the distribution of bamboo joints (Wang & Song, 2022), as shown in Fig 3, the spacing of bamboo joints is uniformly distributed within a certain range. Because the bamboo structure is applied to the web plate, and based on the model’s dimensions, hexagonal bamboo joints are evenly distributed on the web plate. Each honeycomb bamboo joint has a side length of 5 mm. Considering the average distribution of bamboo joints and the length of the web plate, the structure is implemented by applying three standard honeycomb hexagonal shapes, with each bamboo joint positioned at 12 mm intervals. Figure 4 presents the bionic blade modeling diagram.

## 2.3 Numerical Modeling in Fluid

### 2.3.1 Computational Domain and Boundary Conditions

The computational domain consists of two parts: the rotational domain, which is inside the stationary domain, and the rotational domain, which transfers information through the contact surfaces of the two domains. The diameter ( $D$ ) of the rotating field is 3 m, with a thickness of 0.4 m, while the length of the static field is 12 m, and

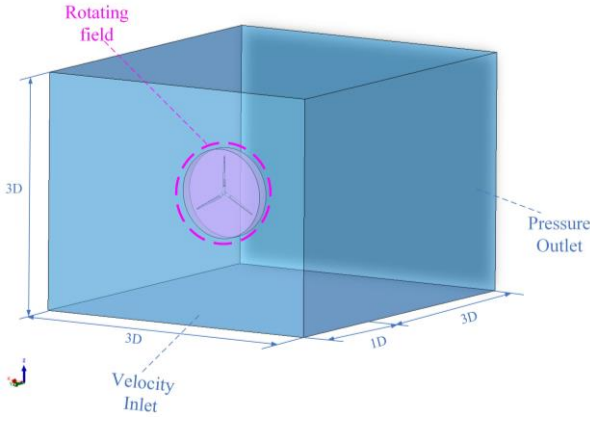


**Fig. 5 Computational domain**

**Table 2 Computational domain independence study**

Computational domain size Width × Height × Length	Power/W	$C_p$
2D × 2D × 3D	1,818	40.2%
3D × 3D × 4D	1,869	41.3%
4D × 4D × 5D	1,875	41.4%

its width and height are both 3D. The rotating center is positioned 1D from the inflow inlet of the static field and 3D from the pressure outlet. The upstream boundary of the static region serves as the velocity inlet, with an inlet speed set to 11.4 m/s. The pressure value at the pressure outlet is set to standard atmospheric pressure, and the other four planes are symmetrical planes. Figure 5 illustrates the computational domain.

The establishment of the computational domain size in this paper is based on relevant literature and previous studies (Wang et al., 2023). By selecting an appropriate computational domain size, a balance between computational accuracy and efficiency can be achieved. To verify the impact of computational domain size on the numerical simulation of wind turbines, three different domain sizes are tested. The distance from the velocity inlet to the rotating domain remains fixed at 1D, while the stationary domain size is gradually increased. As observed in Table 2, when the computational domain is too small, the results lack accuracy. Conversely, when the domain is excessively large, the computation time becomes significantly longer; however, the improvement in results is minimal, leading to unnecessary computational resource consumption. Therefore, the optimal computational domain size selected in this paper is 3D × 3D × 4D.

### 2.3.2 Turbulence Model and Calculation Methods

In this study, CFD numerical simulation is conducted using ANSYS Fluent commercial software. The choice of turbulence model influences both the accuracy of the simulation results and the ability of the simulation process to converge. The SST  $k-\omega$  turbulence model integrates the advantages of two other models: first, the  $k-\omega$  model provides high simulation accuracy for near-wall fluid flow, and second, the  $k-\varepsilon$  model effectively simulates turbulence in the free-flow region. Garcia-Ribeiro et al. (2023) evaluated multiple turbulence models and found

that the SST  $k-\omega$  model requires minimal additional computational cost while delivering more accurate results than alternative turbulence models. Consequently, the SST  $k-\omega$  model is adopted in this study, with the SIMPLE algorithm selected as the numerical method. In addition, a second-order upwind scheme is used for the convective term discretization. During the solution process, the residual value is set to  $1 \times 10^{-4}$ . The SST  $k-\omega$  turbulence model, including the eddy coefficients,  $k$  equation, and  $\omega$  equation, is expressed as follows:

$$v_t = \frac{a_1 k}{\max(a_1 \omega; \Omega F_2)} \quad (1)$$

$$\frac{D\rho k}{Dt} = \frac{\partial}{\partial x_j} \left[ (\mu + \sigma_k \mu_t) \frac{\partial k}{\partial x_j} \right] + \tau_{ij} \frac{\partial \mu_i}{\partial x_j} - \beta^* \rho \omega k \quad (2)$$

$$\text{where } \tau_{ij} = -\rho u'_i u'_j$$

$$\frac{D\rho k}{Dt} = \frac{\partial}{\partial x_j} \left[ (\mu + \sigma_k \mu_t) \frac{\partial k}{\partial x_j} \right] + \tau_{ij} \frac{\partial \mu_i}{\partial x_j} - \beta^* \rho \omega k \quad (3)$$

where  $\Omega$  is the vortex volume,  $F_1 = \tanh(\arg 2^2)$ ,

$\arg 2 = \max \left[ 2 \frac{\sqrt{k}}{0.09 \omega y}; \frac{500 \nu}{y^2 \omega} \right]$ ;  $y$  is the distance from the wall.

In engineering applications, the Reynolds-averaged Navier–Stokes (RANS) method is currently the most established approach and is well-suited for this study due to its accuracy and computational efficiency. The RANS method employs the Navier–Stokes (N–S) equations as the governing equations for flow field simulation, expressed as follows:

$$\frac{\partial \mathbf{Q}}{\partial t} + \frac{\partial (\mathbf{F}_i + \mathbf{F}_v)}{\partial x} + \frac{\partial (\mathbf{G}_i + \mathbf{G}_v)}{\partial y} + \frac{\partial (\mathbf{H}_i + \mathbf{H}_v)}{\partial z} = 0 \quad (4)$$

where:  $\mathbf{Q} = (\rho, \rho u, \rho v, \rho w, \rho E)^T$  is a vector of conserved variables,  $\mathbf{F}_i$ ,  $\mathbf{G}_i$ ,  $\mathbf{H}_i$  are the flux vector of convection term.,  $\mathbf{F}_v$ ,  $\mathbf{G}_v$ ,  $\mathbf{H}_v$  are viscous term flux vectors.

### 2.3.3 CFD Mesh and Model Validation

The meshing process in this study is performed using ANSYS Meshing commercial software. The grid size and type must be carefully selected to ensure computational efficiency and accuracy. An unstructured polyhedral core grid is utilized for grid division. To refine the boundary layer mesh density, the boundary layer grid near the wall is set to satisfy  $y^+ < 1$ , with the first mesh thickness set to 0.01 mm, totaling 15 boundary layers. The blade surface mesh is further refined. Fig 6 depicts the meshing of the blade and fluid field.

$$y^+ \equiv \frac{u_* y}{\nu} \quad (5)$$

where  $u_*$  is the friction velocity at the nearest wall,  $y$  is the distance to the nearest wall, and  $\nu$  is the local kinematic viscosity of the fluid.

Grid size significantly impacts simulation accuracy. In this study, five different grid configurations are tested to assess grid adequacy. As shown in Fig 7, torque values increase as grid refinement progresses. When the number of grids reaches 9.3 million, the torque value aligns with the blade design. However, when the grid count exceeds 9.3 million, the improvement in accuracy is marginal.

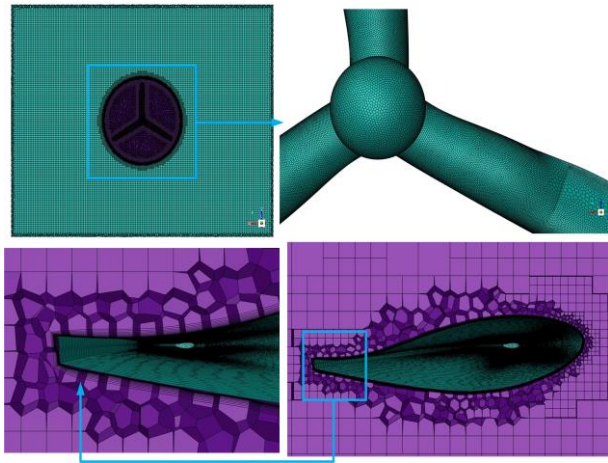


**Fig. 6 Blade and fluid domain mesh**

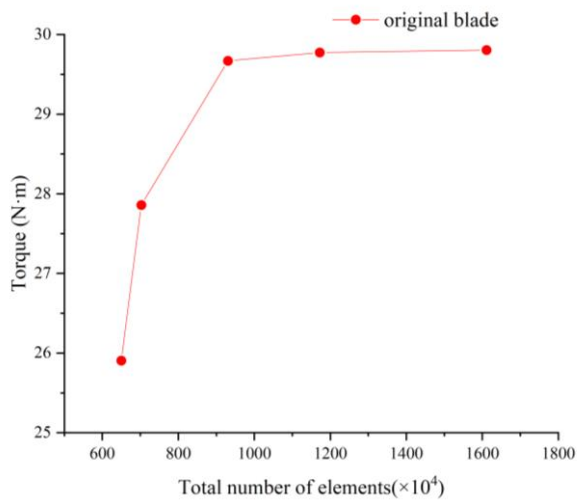


**Fig. 7 Verification of grid independence**

Considering the substantial increase in computational time and cost beyond 9.3 million grids, the tradeoff between accuracy and computational efficiency is evaluated. Consequently, in this study, 9.3 million grids is selected as the optimal configuration.

Comparing the torque calculated by CFD with the design value, the blade’s design torque in this study is 32 N·m, while the torque calculated by CFD is 29.67 N·m. After calculation, the designed power  $P$  of the blade is 2000 W, with a designed power coefficient  $C_p$  of 44.2%. The blade power obtained from CFD numerical simulation is 1,869 W, with a power coefficient  $C_p$  of 41.3%. Compared to the design values, the power and power coefficient errors of the CFD numerical simulation are 6.5% and 2.9%, respectively. Power output validation was

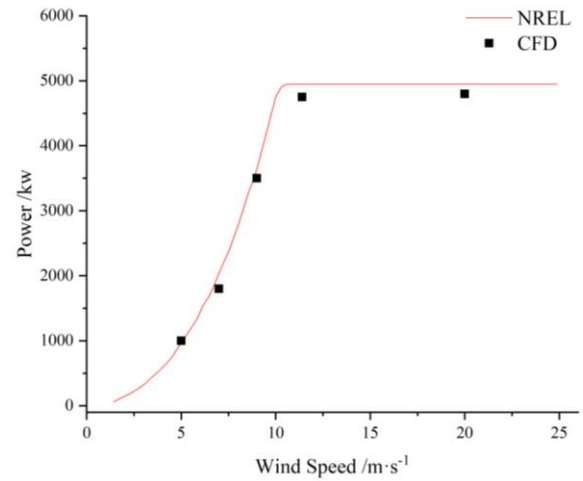


**Fig. 8 Wind turbine power comparison**

performed across five wind speed regimes: 5, 7, 9, 11.4, and 20 m/s. The power was converted using the power criterion from Table 1, Similarized Parameters, and compared with power data from NREL (Jonkman et al., 2009). As shown in Fig 8, the power obtained from the model in this study closely matches the NREL data, with minimal error. CFD results validate the feasibility of the model.

The power coefficient  $C_p$  is calculated as follows:

$$C_p = \frac{T\omega}{0.5\rho\pi R^2v^3} \quad (6)$$

where  $\rho$  is the density of air,  $\text{kg/m}^3$ ;  $R$  is the radius of the wind turbine wind wheel, m;  $v$  is the incoming velocity, m/s.

## 2.4 Numerical Modeling in Structure

### 2.4.1 Material Properties

Wind turbines experience significant aerodynamic loads during operation, making their design crucial not only for ensuring high strength but also for achieving lightweight construction and utilizing abundant material resources. Therefore, selecting appropriate materials for wind turbine blades is essential. E-glass fibers are widely used in engineering applications due to their cost-effectiveness and favorable mechanical properties. In this study, the blade is made of E-glass fiber. For comparative analysis of overall vibration performance, E-glass fiber is modeled as isotropic, even though composite materials are inherently anisotropic. This simplification aligns with the study’s focus on preliminary design validation and computational efficiency (Ertorun et al., 2024). Table 3 presents the material properties of E-glass fiber.

**Table 3 E-glass fiber Material properties**

Material	Density/g $\text{cm}^{-3}$	Young’s modulus/GPa	Bulk modulus GPa	Shear modulus GPa	Allowable stress/MPa	Poisson ratio
E- glass fiber	2.54	73	43.452	29.918	686	0.22

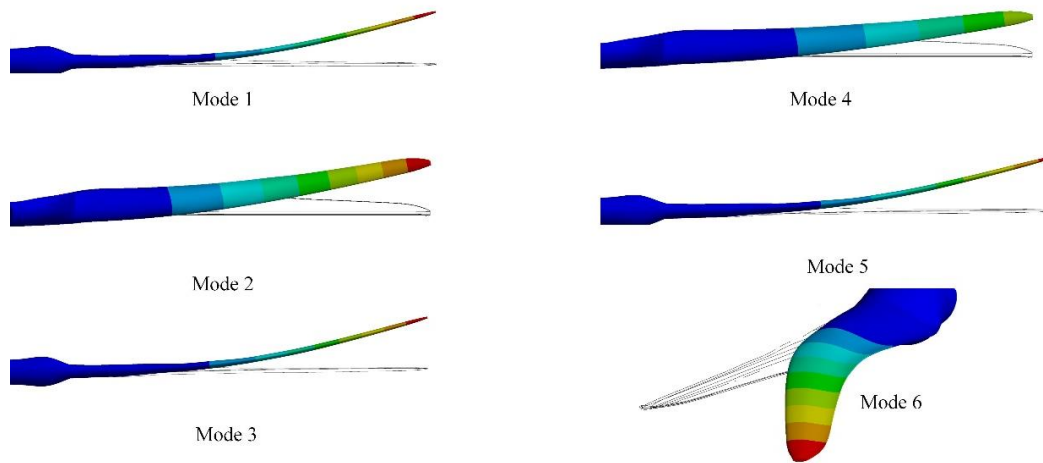


**Fig. 9** First to sixth modal shapes of the blade

**Table 4** Modal Frequency Comparison

Model#	Frequency (Hz)		Diff
	Ansys (Resor, 2013)	Present model	
1	0.87	0.86	-1.15%
2	1.06	1.09	+2.83%
3	2.68	2.62	-2.24%
4	3.91	3.95	+1.02%
5	5.57	5.63	+1.08%
6	6.45	6.40	-0.78%

### 2.4.2 FEA Mesh

In this study, FEA numerical simulation is conducted using ANSYS Mechanical commercial software. The wind turbine blade is meshed with tetrahedral unstructured meshing, which is necessary for detailed meshing of narrow blade sections. In the Transient Structural module, the number of mesh elements for the blade reaches 3.1 million, with an average mesh mass of 0.8 and an average skewness of 0.26, ensuring that the mesh quality meets the required standards.

In addition to the aerodynamic load obtained from the CFD simulation, the centrifugal load generated by the blade’s rotation is also considered. The bionic wind turbine operates at a rotational velocity of 605 r/min. During the simulation, the wind turbine blades must be fixed within the rotational domain, and displacement constraints must be applied at the hub. The blade’s response under specified load conditions is analyzed using linear static analysis, with the general dynamic equation for wind turbine blades expressed as follows:

$$[M]\{\ddot{x}\} + [C]\{\dot{x}\} + [K]\{x\} = \{F(t)\} \quad (7)$$

$[C]$  is the damping matrix;  $[K]$  is the stiffness coefficient matrix;  $\{x\}$  is the displacement vector; and  $\{F\}$  is the force vector.

In the linear static analysis, the time variable is neglected and reduced to:

$$[M]\{x\} = \{F\} \quad (8)$$

### 2.4.3 FEA Model Validation

To ensure the accuracy of the FEA model, this study conducted modal analysis on a 5MW 1:1 scale model. By fixing the blade root as the boundary condition, the first six modal shapes of the FEA model were obtained, as shown in Fig 9. The first, third, and fifth modes corresponded to flap-wise vibrations, while the second and fourth modes represented edge-wise vibrations. The sixth mode exhibited torsional vibration. The modal frequencies of the blade were obtained and compared with results from the literature Ansys (Resor, 2013), as summarized in Table 4. The maximum frequency error occurred in the second mode (2.83%), which confirms the validity of the FEA model.

### 2.5 Fluid–Solid Interaction Theory

The software used for fluid–solid coupling is ANSYS Workbench, where the coupling process integrates ANSYS Fluent and ANSYS Mechanical. Figure 10 presents the one-way fluid–solid interaction solution. Contemporary FSI methodologies primarily fall into two categories: the directly coupled solution and the partitioned solution, the latter of which is applied in this study. In this approach, calculation results are transferred iteratively between the fluid and solid domains via the fluid–solid interface. Once convergence is achieved, the next calculation is performed in sequence. In one-way fluid–solid interaction, both fluid and solid solutions must adhere to fundamental conservation principles. Therefore, at the fluid domain and solid interface, parameters such as atmospheric pressure, blade stress, displacement, flow,

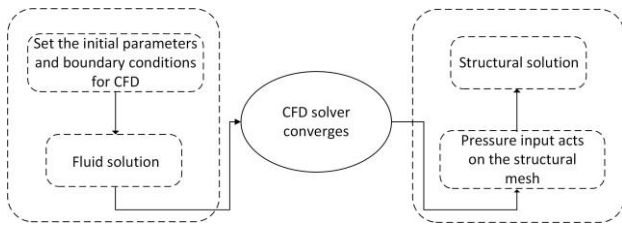


**Fig. 10 One-way interaction solution**

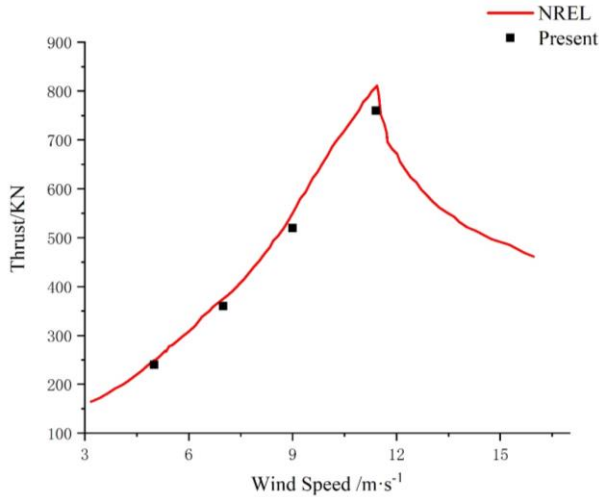


**Fig. 11 Thrust comparison under FSI**

and temperature must be conserved, satisfying the following equations:

$$\begin{aligned} \tau_f \cdot n_f &= \tau_s \cdot n_s \\ d_f &= d_s \\ q_f &= q_s \\ T_f &= T_s \end{aligned} \quad (9)$$

where  $\tau$  is the stress,  $d$  is displacement,  $q$  is heat flux,  $T$  is temperature,  $f$  is fluid, and  $s$  is blade solid.

### 2.5.1 FSI Validation

The thrust under the coupled model was monitored through simulation at wind speeds of 5, 7, 9, and 11.4 m/s. A thrust comparison diagram (Fig. 11) was generated. By comparing the results with data from the NREL official report, the maximum error of the simulated thrust was found to be only 6.06%. The simulation deviations fall within acceptable limits, thereby validating the accuracy of the coupled model.

## 3. RESULTS AND DISCUSSIONS

### 3.1 Deformation Analysis

As shown in Fig. 12, the displacement diagram indicates that blade deformation increases progressively from the blade root to the blade tip. At the blade root, displacement is minimal, with negligible differences between the blades. However, from the root to the middle region, displacement variation becomes more pronounced.

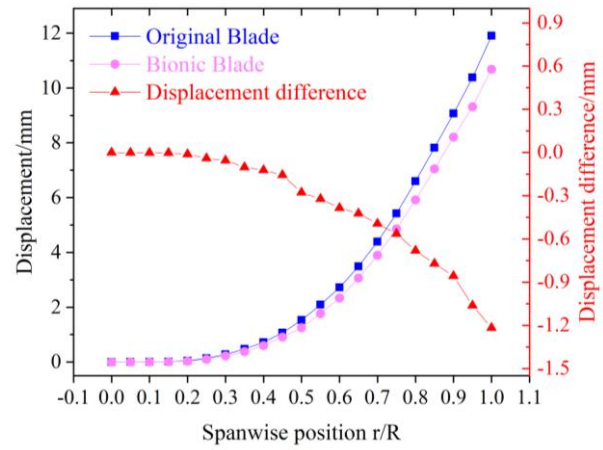


**Fig. 12 Displacement distribution of original and bionic blades**

The original blade exhibits greater deformation than the bionic blade, with maximum deformation occurring at the blade tip. The tip displacement of the original blade is 11.917 mm, whereas that of the bionic blade is 10.718 mm, resulting in a 10.1% reduction in peak displacement amplitude for the biomimetic blade compared to the conventional design. This demonstrates that the bamboo honeycomb web structure of the bionic blade significantly enhances deformation resistance, improves bending resistance, and enhances overall performance for safe operation.

### 3.2 Stress and Strain Analysis

#### 3.2.1 Web Analysis

As shown in Fig. 13, the stress cloud diagrams of the original web and the bamboo honeycomb web are compared. By conducting static analysis on both webs independently, the functional mechanism of the bamboo honeycomb web can be examined more intuitively. With one end of the webs fixed, a pressure of 0.0037835 MPa in the -Y direction, derived from FSI analysis, is applied to simulate wind loads during turbine operation. Figure 11 indicates that the bamboo honeycomb web demonstrates stress buffering and a more uniform stress distribution than the original web. A path AB was defined 17 mm below the top surface of the webs, and Fig 14 illustrates the stress distribution along this path. The results show that under identical conditions, the bamboo honeycomb web experiences lower stress levels with a gradual reduction trend, effectively mitigating damage caused by abrupt stress variations. This improvement is attributed to the hierarchical buffering mechanism of the hexagonal honeycomb structure at bamboo nodes, which progressively dissipates wind impact and reduces stress. The study confirms that bamboo honeycomb webs significantly enhance structural stress performance under equivalent loading conditions.

#### 3.2.2 Blade Analysis

Figure 15 shows the stress cloud of the original blade and the bionic blade. From the colors in the figure, the stress distributions are found to be very similar, with only

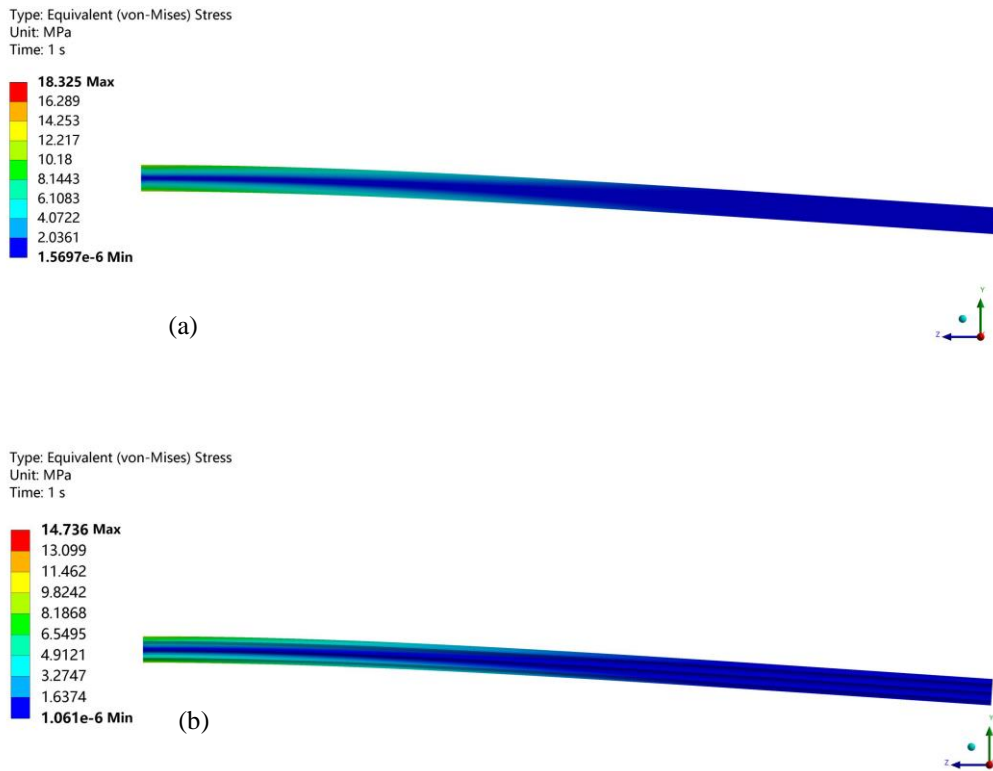


**Fig. 13 Stress cloud diagram. (a) Original Web (b) Bamboo Honeycomb Web**

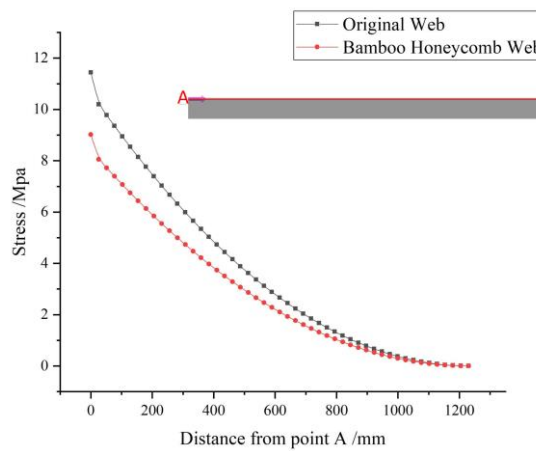


**Fig. 14 Stresses along Path AB in the Original Web and Bamboo Honeycomb Web**

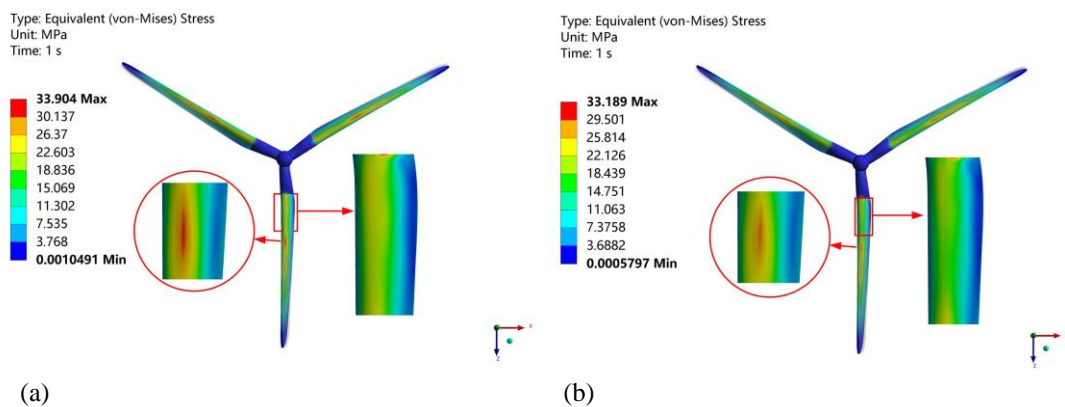


**Fig. 15 Stress cloud diagram (a) Original Blade (b) Bionic Blade**

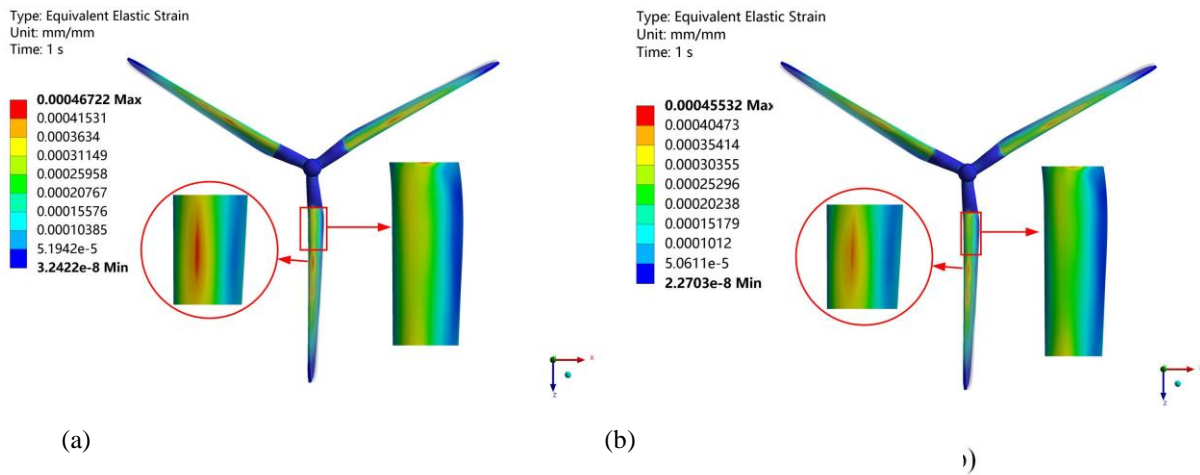


**Fig. 16 Strain cloud diagram (a) Original Blade (b) Bionic Blade**

minor differences in some areas. In both the original and bionic blades, the stresses are generally greater at the leading edge than at the trailing edge, becoming progressively smaller. The stresses experienced in the middle of the blade are the highest, while they decrease gradually toward the blade tip. The blade root exhibits the minimum stress value, which is attributed to its cylindrical cross-section and proximity to the hub, where the force applied is greater than at 50% of the blade length. Assuming the blade length to be 100%, the maximum stress value occurs at 45% of the blade length in an elliptical region. The maximum stress value of the original blade is 2.1% higher than that of the bionic blade. In the localized magnified view at 45% of the blade, the bionic blade demonstrates a reduced maximum stress area compared to the original blade, along with a narrower range of peak stress values. After calculations, the elliptical domain of maximum stress in the original blade was measured to be 50.5% larger than that of the bionic blade. Examining the localized magnified stress cloud map in the 30%–40% region of the blade, the bionic blade shows a reduction in stress values in this area. This indicates that the bionic web plays a key role, likely because the bamboo joints in the bamboo honeycomb web cushion wind loads, transferring them in phases, with each joint absorbing a portion of the wind loads. The bamboo honeycomb web effectively reduces stress values, enhancing the safe operation of the wind turbine blade.

Figure 16 presents the strain clouds of both blades. The stress and strain distribution regions in Fig. 15 and Fig. 16 remain consistent with little variation. However, the original blade’s maximum strain value is 2.5% higher than that of the bionic blade.

First, the bionic blade design improves the fatigue life of the blade by optimizing its structure, making the stress distribution more uniform and reducing stress concentration. Second, the reduction in stress and strain delays the accumulation of fatigue damage, effectively minimizing long-term fatigue damage and improving the blade’s durability. In addition, reducing stress and strain lowers the risk of blade damage, decreasing the frequency of repairs and replacements.

### 3.3 Modal Analysis

Modes define the intrinsic properties and vibration characteristics of a structural system, and modal analysis provides a deeper understanding of the structure’s dynamic behavior. Figure 17 illustrates the first six modal orders of both blades. A comparison of the vibration patterns between the original and bionic blades reveals that the first three vibration modes are identical, all exhibiting flap-wise vibrations. The fourth and fifth modes correspond to edge-wise vibrations, while the sixth mode represents torsional vibration. As the primary energy of blade vibration is concentrated in the lower-order modes, this study focuses on flap-wise vibration as the dominant mode. The modal displacements of the bionic blade are consistently lower, whereas those of the original blade are higher, regardless of the vibration mode order. This confirms that the bionic blade exhibits better deformation resistance than the original blade.

To avoid resonance and ensure safe operation, the wind turbine blade’s intrinsic frequency must avoid 1P and 3P across the frequency variation range, maintaining a relative difference of at least 10%. If this condition is met, the wind turbine can operate normally.

Wind turbine operating frequency  $f$  (Hz) is

$$f = \frac{n}{60} \quad (10)$$

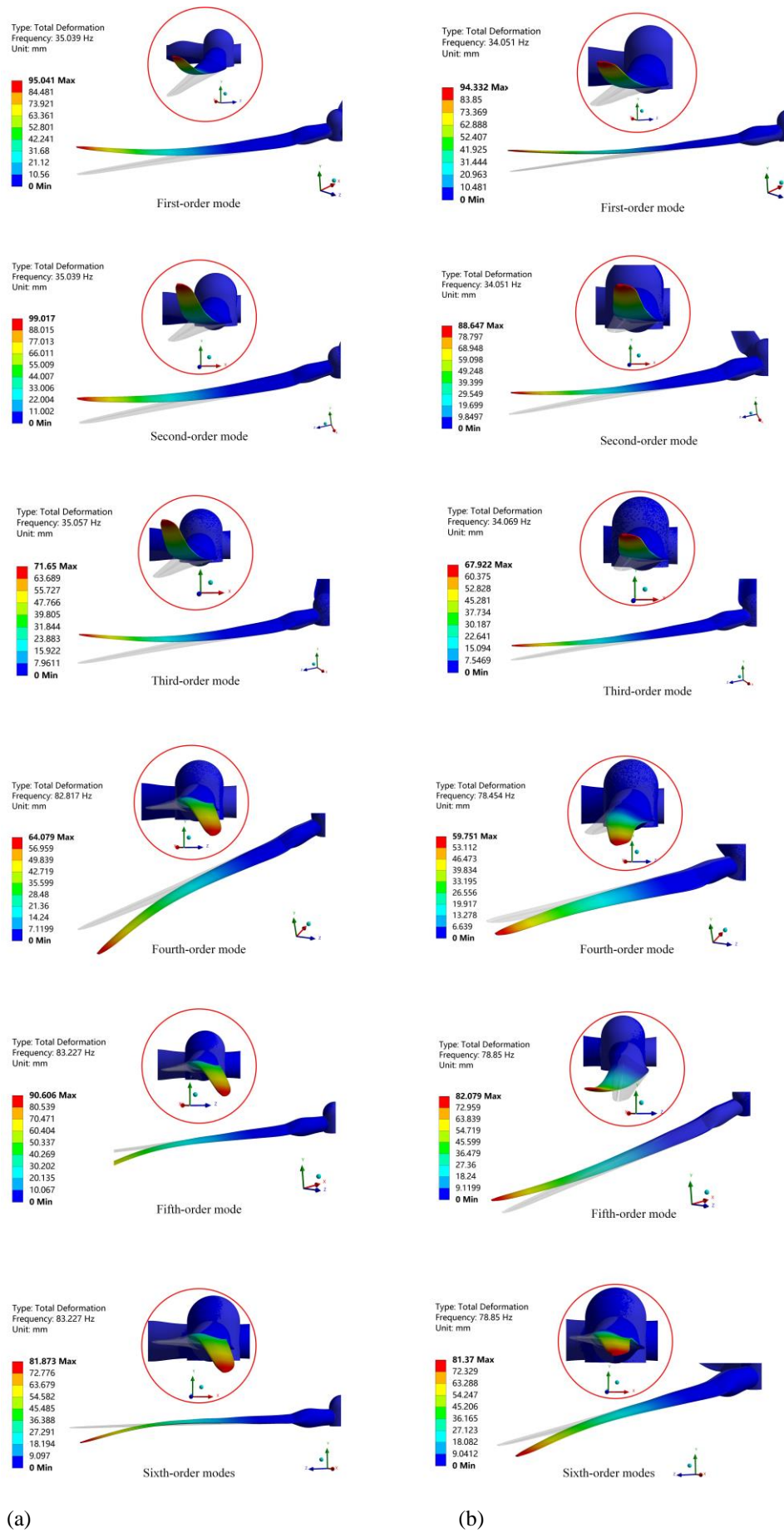
where  $n$  is the rated velocity of the wind turbine, r/min.

The relative difference between the intrinsic frequency and the operating frequency  $R$ , is

$$R = \frac{f_i - f}{f} \quad (11)$$

where  $f_i$  is the intrinsic frequency of each stage, Hz.

The designed wind turbine has a rated speed of 605 r/min. Using the above equation, the corresponding blade rotational frequencies, 1P and 3P, are calculated as 10.08 Hz and 30.24 Hz, respectively. The intrinsic frequency of the bionic blade at each stage exhibits a relative difference from the 1P and 3P frequencies that exceeds 10%.



(a)

(b)

**Fig. 17 First to sixth-order modes  
(a) Original Blade (b) Bionic Blade**

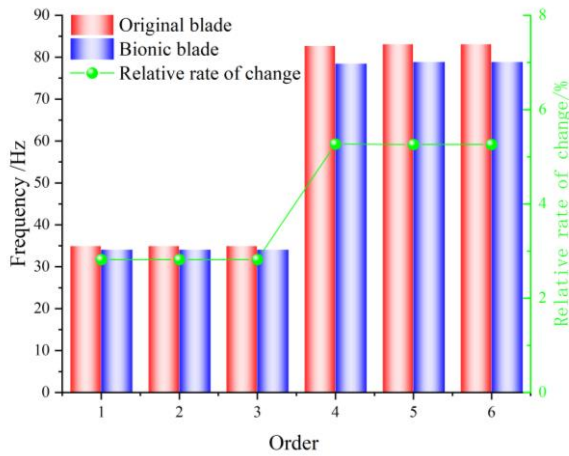


**Fig. 18 First six orders of intrinsic frequency and relative variation**

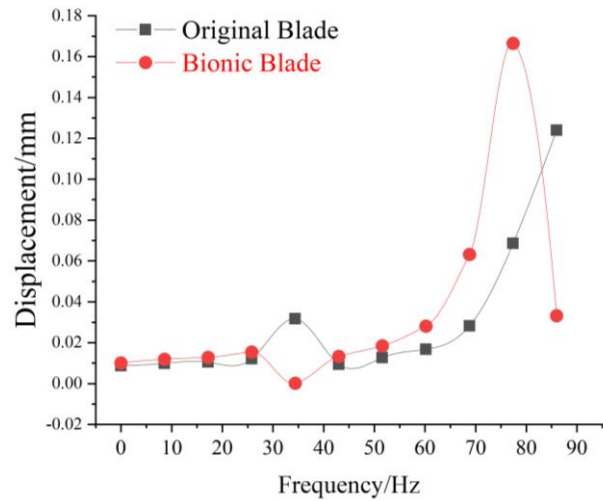
confirming that resonance will not occur and that the blade structure is safe.

Figure 18 presents the first six intrinsic frequencies and their relative variations for both blades, with the bionic blade serving as the reference. From the first to the sixth order, the modal frequencies of both blades gradually increase. The bionic structure alters the intrinsic frequencies, resulting in lower sixth-order intrinsic frequencies in the bionic blade. These changes occur because the bionic structure modifies the original mass and stiffness distribution, which in turn influences the structural stiffness matrix in the dynamic equation. The bamboo honeycomb web has minimal impact on the first three modal orders of the bionic blade but significantly affects the last three orders.

### 3.4 Harmonic Response Analysis

Harmonic response analysis is a crucial methodology in structural dynamics, used to examine the vibrational characteristics of engineering systems subjected to sustained sinusoidal load excitation. It provides theoretical support for vibration-resistant design and fatigue life prediction in engineering applications. This method is widely employed in the design and analysis of rotating machinery and structures affected by eddy currents.

Harmonic response analysis is a fundamental tool for structural designers to assess and mitigate resonance phenomena, fatigue accumulation, and vibration-induced failure mechanisms, thereby ensuring structural integrity and operational reliability under cyclic excitation conditions (Li et al., 2011). This simulation employs the modal response method. Based on the first six intrinsic modal frequencies of the blade, the swept frequency range for harmonic response analysis is set to 0–86 Hz. In this study, the blade undergoes flap-wise vibration, edge-wise vibration, and torsional deformation. Among these, flap-wise vibration has the highest percentage. The original blade exhibits a natural frequency of 35.039 Hz, while modal analysis of the bionic blade reveals a natural frequency of 34.051 Hz. The analysis primarily focuses on flap-wise vibration for both blade types.



**Fig. 19 Displacement response with frequency**

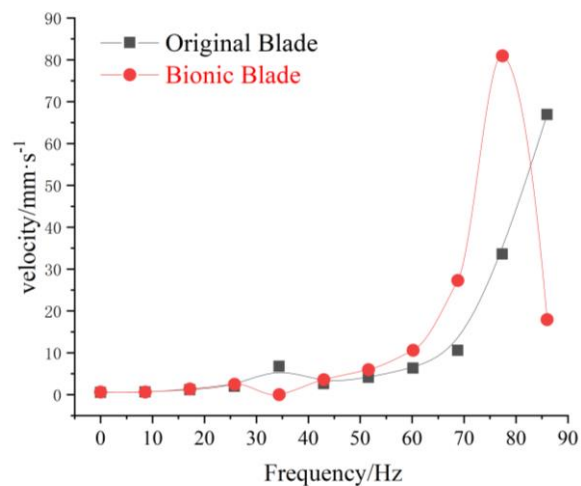


**Fig. 20 Velocity response with frequency**

As shown in Fig. 19, the displacement versus frequency curves for both blades under flap-wise vibration are presented. In an overall comparison with the original blade, within the 0–28 Hz range, the bionic blade’s displacement response is slightly larger. However, around the intrinsic frequency of 34 Hz, the bionic blade’s displacement response begins to decrease, with values reduced by 99.58%. Between 42–68 Hz, the bionic blade’s displacement response increases. From 68–78 Hz, the displacement response rises rapidly, reaching a peak value of 0.0317 mm at 78 Hz. At 82–86 Hz, the displacement response of the bionic web decreases sharply.

As shown in Fig. 20, the velocity versus frequency curves for both blades under flap-wise vibration are displayed. In the overall comparison with the original blade, within the 0–28 Hz range, there is no difference in velocity response between the two blades. Near the intrinsic frequency of 34 Hz, the velocity response decreases by 99.55%. Between 42–68 Hz, the velocity response of the bionic blade increases. From 68–78 Hz, the velocity response rises rapidly, peaking at 78 Hz. At

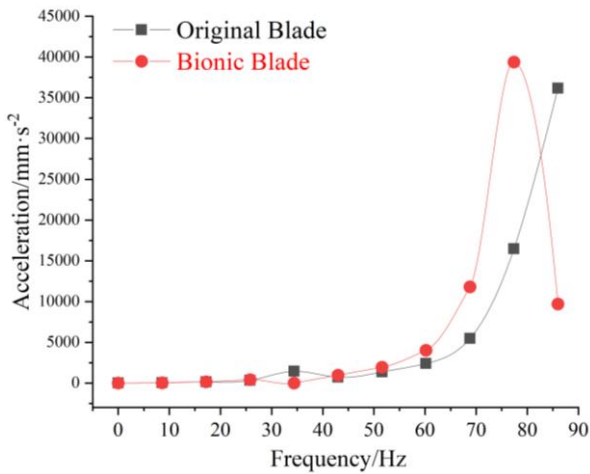


**Fig. 21 Acceleration response with frequency**

82–86 Hz, the velocity response of the bionic blade gradually decreases.

As shown in Fig. 21, the acceleration versus frequency curves for both blades under flap-wise vibration are presented. In the overall comparison with the original blade, within the 0–28 Hz range, there is no difference in acceleration response between the two blades. Near the intrinsic frequency of 34 Hz, the bionic blade’s acceleration response decreases by 99.55%. Between 42–68 Hz, the acceleration response of the bionic blade increases. From 68–78 Hz, the acceleration response rises rapidly, peaking at 78 Hz. At 82–86 Hz, the acceleration response gradually decreases.

After conducting harmonic response analysis, it is observed that the displacement, velocity, and acceleration responses under flap-wise vibration for the blade equipped with bamboo honeycomb webs are lower than those of the original blade at the first three intrinsic frequency orders. The vibration amplitude of both wind turbine blades increases dramatically, peaking at the third-highest intrinsic frequency order. Therefore, under operational conditions, excitation forces near the latter third-order intrinsic frequency should be avoided, and the wind turbine’s operating frequency should not be excessively high to prevent resonance. The primary vibration mode is first-order flap-wise vibration, and the blade resonates only when its frequency matches the intrinsic frequency. The bionic blade significantly reduces the response at resonance, greatly enhancing its vibration resistance and ensuring safe wind turbine operation.

#### 4. CONCLUSION

In response to the demand for enhanced structural performance in large-scale wind turbines, this paper proposes a bionic wind turbine blade that leverages the functional similarities between web plate structures and bamboo. By incorporating bamboo and honeycomb structures into the web plate, the following analyses were conducted: deformation analysis, stress-strain analysis, modal analysis, and harmonic response analysis, using the

fluid–solid interaction method. The key conclusions are as follows:

(1) Underrated operating conditions, the maximum deformation displacement of the bionic blade is reduced by 10.1% compared to the original blade. The bionic web effectively disperses concentrated wind loads through the graded buffering mechanism of its bamboo-joint-inspired honeycomb structure, enhancing the blade’s bending stiffness. This improvement reduces blade tip displacement amplitude and mitigates the risk of fatigue crack initiation under dynamic loads.

(2) In stress–strain analysis, the bionic blade exhibits reductions of 2.1% and 2.5% in maximum surface stress and strain, respectively. The elliptical stress concentration zone at the 45% span-wise position is 50.5% smaller in the bionic blade than in the original blade. This indicates that the bioinspired structure significantly enhances stress distribution uniformity while reducing localized failure susceptibility.

(3) In modal analysis, the primary vibration patterns for both blades are flap-wise and edge-wise vibrations. The modal displacement deformation values of the bionic blade are consistently smaller, demonstrating better deformation resistance. The relative differences between the intrinsic frequencies and the 1P and 3P frequencies at each stage exceed 10%, effectively preventing resonance and ensuring operational safety.

(4) Under first-order flap-wise resonance frequency conditions, the bionic blade exhibits reductions of 99.58%, 95.55%, and 95.54% in displacement, velocity, and acceleration response peaks, respectively, compared to the original blade. This improvement results from the synergistic effects of the bamboo-joint-inspired honeycomb structure within the bionic web, where the bioinspired configuration’s damping properties effectively suppress resonance amplitudes.

#### PROSPECTS

In manufacturing bionic blades, composite material forming technology can be employed to simulate bamboo structures. The bamboo honeycomb structure can be fabricated using mold-forming processes. The processing of bamboo and the design of honeycomb structures are relatively straightforward, allowing existing material processing techniques to be applied in production. Incorporating the bamboo honeycomb structure not only enhances blade strength and stiffness but also disperses stress concentrations, reducing the risk of fatigue crack initiation and propagation. The bionic blade demonstrates superior displacement, stress, and strain performance under load compared to traditional blades, indicating better durability under dynamic loads. The buffering characteristics of the bionic structure help mitigate fatigue and damage under extreme climatic conditions.

First, in terms of materials, long-term partnerships with suppliers should be established to ensure a stable supply of raw materials and cost-effectiveness. Second, mold design for manufacturing bionic blades should be optimized to minimize material waste and increase

production efficiency. In addition, proactive marketing strategies should be implemented to promote bionic blades. Large-scale production can also be facilitated through government support for renewable energy technology development. By implementing these strategies, the commercialization and widespread adoption of bionic blades can be effectively promoted, contributing to the advancement of the wind energy industry and the realization of sustainable energy goals.

From a cost-effectiveness perspective, E-glass fiber, one of the primary materials used in bionic blade manufacturing, has a relatively low cost, which can be further reduced through bulk purchasing in mass production. In terms of manufacturing costs, the introduction of automated production equipment and processes can significantly enhance efficiency while reducing labor costs. Regarding maintenance and operational expenses, the durability of bionic blades and their reduced stress levels result in less frequent maintenance, thereby lowering maintenance costs. Environmentally, the adoption of bionic design concepts fosters greater environmental awareness, promotes the application of green technologies, and has the potential to drive the entire industry toward more sustainable practices.

The isotropic model and von Mises criterion used in this study may underestimate local stress concentration effects in composite materials. Future research should incorporate anisotropic failure criteria for a more accurate assessment of blade fatigue lifespan and failure susceptibility.

#### ACKNOWLEDGEMENTS

This work was supported by the National Natural Science Foundation of China (No. 52205286), the Natural Science Foundation of Xinjiang Uygur Autonomous Region (No. 2022D01C33) and the Graduate Research Innovation Project of Xinjiang Uygur Autonomous Region (No. XJ2024G091).

#### CONFLICT OF INTEREST

The authors in this work declared that there is no conflict

#### AUTHORS CONTRIBUTION

**Tao Su:** Investigation; Writing–original draft. **Kun Chen:** Data curation; Writing–review & editing; **Qi Wang:** Visualization; **Zhikai Zhao:** Validation; **Hongyi Hu:** Project administration

#### REFERENCES

Barr, S. M., & Jaworski, J. W. (2019). Optimization of tow-steered composite wind turbine blades for static aeroelastic performance. *Renewable Energy*, 139, 859–872. <https://doi.org/10.1016/j.renene.2019.02.125>

Choi, D. K., An, H. J., Lee, S. Y., & Bae, J. S. (2022). Fluid–Structure Interaction Analysis of a Fabric Skin for Fabric-Covered Wind Turbine Blades. *International Journal of Aeronautical and Space Sciences*, 23(1), 92–101. <https://doi.org/10.1007/s42405-021-00419-2>

Deng, Z., Xiao, Q., Huang, Y., Yang, L., & Liu, Y. (2024). A general FSI framework for an effective stress analysis on composite wind turbine blades. *Ocean Engineering*, 291, 116412. <https://doi.org/10.1016/j.oceaneng.2023.116412>

Ertorun, E. M., Yayla, M., Isik, D., & Cadirci, S. (2024). One-way fluid–structure interaction modeling and multi-objective optimization of horizontal-axis wind turbine blades equipped with winglets. *International Journal of Green Energy*, 1–17. <https://doi.org/10.1080/15435075.2024.2430432>

Garcia-Ribeiro, D., Malatesta, V., Moura, R. C., & Cerón-Muñoz, H. D. (2023). Assessment of RANS-type turbulence models for CFD simulations of horizontal axis wind turbines at moderate Reynolds numbers. *Journal of the Brazilian Society of Mechanical Sciences and Engineering*, 45(11), 566. <https://doi.org/10.1007/s40430-023-04488-0>

Giahi, M. H., & Jafarian Dehkordi, A. (2016). Investigating the influence of dimensional scaling on aerodynamic characteristics of wind turbine using CFD simulation. *Renewable Energy*, 97, 162–168. <https://doi.org/10.1016/j.renene.2016.05.059>

Han, S., He, Y., Ye, H., Ren, X., Chen, F., Liu, K., Shi, S. Q., & Wang, G. (2024). Mechanical behavior of bamboo, and its biomimetic composites and structural members: A systematic review. *Journal of Bionic Engineering*, 21(1), 56–73. <https://doi.org/10.1007/s42235-023-00430-1>

Herrera, C., Correa, M., Villada, V., Vanegas, J. D., García, J. G., Nieto-Londoño, C., & Sierra-Pérez, J. (2019). Structural design and manufacturing process of a low scale bio-inspired wind turbine blades. *Composite Structures*, 208, 1–12. <https://doi.org/10.1016/j.compstruct.2018.08.061>

Huang, S., Qiu, H., & Wang, Y. (2022). Aerodynamic performance of horizontal axis wind turbine with application of dolphin head-shape and lever movement of skeleton bionic airfoils. *Energy Conversion and Management*, 267, 115803. <https://doi.org/10.1016/j.enconman.2022.115803>

Huang, Y., Yang, X., Zhao, W., & Wan, D. (2024). Aeroelastic analysis of wind turbine under diverse inflow conditions. *Ocean Engineering*, 307, 118235. <https://doi.org/10.1016/j.oceaneng.2024.118235>

Huque, Z., Zemmouri, F., Lu, H., & Kommalapati, R. R. (2024). Fluid–Structure interaction simulations of wind turbine blades with pointed tips. *Energies*, 17(5), 1090. <https://doi.org/10.3390/en17051090>

Jonkman, J., Butterfield, S., Musial, W., & Scott, G. (2009). *Definition of a 5-MW Reference Wind Turbine for Offshore System Development* (No.

- NREL/TP-500-38060, 947422; p. NREL/TP-500-38060, 947422). <https://doi.org/10.2172/947422>
- Keprate, A., Bagalkot, N., Siddiqui, M. S., & Sen, S. (2023). Reliability analysis of 15MW horizontal axis wind turbine rotor blades using fluid-structure interaction simulation and adaptive kriging model. *Ocean Engineering*, 288, 116138. <https://doi.org/10.1016/j.oceaneng.2023.116138>
- Li, J., Chen, J., & Chen, X. (2011). Aerodynamic response analysis of wind turbines. *Journal of Mechanical Science and Technology*, 25(1), 89–95. <https://doi.org/10.1007/s12206-010-0909-z>
- Li, W., Xiong, Y., Su, G., Ye, Z., Wang, G., & Chen, Z. (2023). The aerodynamic performance of horizontal axis wind turbines under rotation condition. *Sustainability*, 15(16), 12553. <https://doi.org/10.3390/su151612553>
- Liu, W., Ma, Y., Wang, N., Luo, Y., & Tang, A. (2022). A design of composite spar/shear web with ZPR honeycombs and graded structures for wind turbine blades. *Mechanics of Advanced Materials and Structures*, 29(25), 3633–3645. <https://doi.org/10.1080/15376494.2021.1907004>
- Resor, B. (2013). *Definition of a 5MW/61.5m wind turbine blade reference model*. (Nos. SAND2013-2569, 1095962, 463454; pp. SAND2013-2569, 1095962, 463454). <https://doi.org/10.2172/1095962>
- Shehata, A. S., Barakat, A., Mito, M. T., Aboelsaoud, M., & Khairy, Y. (2024). Wind turbine tip deflection control using bio-inspired tubercle leading edges: Analysis of potential designs. *Journal of Wind Engineering and Industrial Aerodynamics*, 245, 105652. <https://doi.org/10.1016/j.jweia.2024.105652>
- Torregrosa, A. J., Gil, A., Quintero, P., & Cremades, A. (2022). On the effects of orthotropic materials in flutter protection of wind turbine flexible blades. *Journal of Wind Engineering and Industrial Aerodynamics*, 227, 105055. <https://doi.org/10.1016/j.jweia.2022.105055>
- Verma, S., Paul, A. R., & Jain, A. (2022). Performance investigation and energy production of a novel horizontal axis wind turbine with winglet. *International Journal of Energy Research*, 46(4), 4947–4964. <https://doi.org/10.1002/er.7488>
- Wang, B., Li, Y., Gao, S., Shen, K., Zhao, S., Yao, Y., Zhou, Z., Hu, Z., & Zheng, X. (2023). Stability analysis of wind turbine blades based on different structural models. *Journal of Marine Science and Engineering*, 11(6), 1106. <https://doi.org/10.3390/jmse11061106>
- Wang, L., Quant, R., & Kolios, A. (2016). Fluid structure interaction modelling of horizontal-axis wind turbine blades based on CFD and FEA. *Journal of Wind Engineering and Industrial Aerodynamics*, 158, 11–25. <https://doi.org/10.1016/j.jweia.2016.09.006>
- Wang, X., & Song, B. (2022). Application of bionic design inspired by bamboo structures in collapse resistance of thin-walled cylindrical shell steel tower. *Thin-Walled Structures*, 171, 108666. <https://doi.org/10.1016/j.tws.2021.108666>
- Yassen, Y. El. S., Abdelhameed, A. S., & Elshorbagy, K. A. (2023). An examination of hub wind turbine utilizing fluid-structure interaction strategy. *Alexandria Engineering Journal*, 64, 1–11. <https://doi.org/10.1016/j.aej.2022.08.042>
- Zhang, D., Liu, Z., Li, W., Zhang, J., Cheng, L., & Hu, G. (2024). Fluid-structure interaction analysis of wind turbine aerodynamic loads and aeroelastic responses considering blade and tower flexibility. *Engineering Structures*, 301, 117289. <https://doi.org/10.1016/j.engstruct.2023.117289>
- Zhang, Y., Song, Y., Shen, C., & Chen, N. Z. (2023). Aerodynamic and structural analysis for blades of a 15MW floating offshore wind turbine. *Ocean Engineering*, 287, 115785. <https://doi.org/10.1016/j.oceaneng.2023.115785>
- Zhao, P., Chen, K., Feng, W., Gui, H., Gao, R., & Li, Y. (2024). Flutter Characteristics of Wind Turbine Blades with V-Stripe Web. *Journal of Vibration Engineering & Technologies*, 12(2), 2485–2497. <https://doi.org/10.1007/s42417-023-00992-8>
- Zheng, T., Zhao, C., & He, J. (2023). Research on fatigue performance of offshore wind turbine blade with basalt fiber bionic plate. *Structures*, 47, 466–481. <https://doi.org/10.1016/j.istruc.2022.11.082>
- Zheng, X., Yao, Y., Hu, Z., Yu, Z., & Hu, S. (2022). Influence of turbulence intensity on the aerodynamic performance of wind turbines based on the fluid-structure coupling method. *Applied Sciences*, 13(1), 250. <https://doi.org/10.3390/app13010250>